Validation of constitutive modeling of shear banding, threadlike wormlike micellar fluids

Natalie Germann
Fluid Dynamics of Complex Biosystems, School of Life Science Engineering Weihenstephan, Technische Universitüt München, 85354 Freising, Germany

A. Kate Gurnon
Center for Molecular and Enginering Thermodynamics, Department of Chemical and Biomolecular Engineering, University of Delaware, Newark, DE 19716, United States

Lin Zhou
Mathematics Department, New York City College of Technology, Brooklyn, NY 11201, United States

L. Pamela Cook
Department of Mathematics, University of Delaware, Newark, DE 19716, United States

Antony N. Beris and Norman J. Wagner
Center for Molecular and Enginering Thermodynamics, Department of Chemical and Biomolecular Engineering, University of Delaware, Newark, DE 19716, United States

July 1, 2016

1 ABSTRACT

In this work, we assess the capability of two thermodynamically consistent, microstruture-based models to predict the rheology and microstructure of a model wormlike micellar surfactant solution known to exhibit shear banding undergoing transient simple shear and large amplitude oscillatory shear deformations in a cylindrical Couette rheometer. The microstructure of the surfactant solution was simultaneously measured during the rheometric tests using small angle neutron scattering and this data is used along with the bulk rheometry to critically evaluate the models. The first model is a new, two-species model specifically developed for wormlike micelles, whereas the second model is the well-known Giesekus model with solvent and diffusion. The new model accounts for the microstructural dynamics including flow-induced micellar breakage and recombination, which is shown to be necessary to predict some of the measured rheology and microstructure. More species should be included to improve the quantitative comparison with experiments, as well as nonlinear relaxation, as judged by the success of the Giesekus model to represent certain features of the time-dependent data. More experimental research is needed to validate the role of flow-induced breakage in the nonlinear rheology of wormlike micellar surfactant solutions.

[1]Corresponding Author: natalie.germann@tum.de

2 INTRODUCTION

Most constitutive models that have been adopted in the past to study shear-banding wormlike micellar (WLM) solutions were originally developed for polymeric materials [1–4]. These models have the advantage that they are simple and thus, can be numerically solved at low computational costs. However, they do not account for the dynamic breakage and recombination processes inherent in self-assembled micellar solutions. Furthermore, an unphysically large solvent contribution is usually necessary to generate the upturn of the shear stress at large shear rates, which is necessary to admit shear banding states [5]. We note that in the following we treat systems for which there are no instabilities, elastic or otherwise, that lead to an apparent increase in stress at high shear rates (for a discussion of this phenomenon, please refer to Fardin et al. [6] and Calabrese et al. [7]).

During the past decade, a few constitutive models have been developed to capture the 'living' nature of WLMs. Cates [8] was the first author to develop a theory that takes the continuous breakage and reaction kinetics of the WLMs into account. In his subsequent study, he extended his theory to the nonlinear flow regime and proposed a constitutive equation for the extra stress [9]. Spenley et al. [10] demonstrated that Cates's model is capable of predicting a constant stress plateau in the steady-state flow curve, which is an experimental signature of shear banding. Cates's model is restricted to weak flows, where nonlinear effects do not have any direct effect on the reaction rates for chain scission and recombination. The fact that the reaction rates are assumed to be constant may be the reason why Cates's model cannot describe strongly nonlinear effects such as the damped oscillations observed in various WLM systems during the start-up of a simple shear flow [11, 12]. Furthermore, in Cates's model, shear banding is associated with the shear-induced tube alignment of the micellar species and not caused, as one may anticipate, by the 'living' nature of WLMs [13]. Zou and Larson [14] extended Cates's theory by accounting for constraint release, bending modes, and a cross-over to the tight entanglement regime. Furthermore, they developed a pointer algorithm that allows to estimate the micellar parameters more quantitatively. Subsequently, they determined the values of multiple characteristic lengths and time constants by fitting the simulation-based mesoscopic model to linear rheological data [15]. Whereas such an approach is very powerful in estimating important micellar parameters, the huge computational requirements limit its applicability in nonlinear rheology.

Inspired by Cates's theory and by using kinetic theory arguments, Vasquez et al. [16] were the first authors to develop such a model for the rheology more generally. In the VCM (Vasqeuz-Cook-McKinley) model, the WLMs are represented by two different species. Species A represents the micelles that are longer than the statistical average in the equilibrium state of rest whereas the shorter micelles are represented by species B. One species A is allowed to break in half to form two species B, which can recombine to form one species A to satisfy detailed balance. To account for a wider size distribution, Grmela et al. [17] extended the VCM model by introducing a third species. This additional species arises by attaching two species A at a fixed angle. More recently, Germann et al. [18] employed a thermodynamic description of the chemical reaction kinetics in viscoelastic media to develop a thermodynamically consistent two-species model that closely resembles the VCM (Vasquez-Cook-McKinley) model. Nonequilibrium thermodynamics requires the transport coefficients appearing in the time evolution equations for the state variables to depend only on the state variables of the system and their spatial derivatives. The VCM model is thermodynamically inconsistent because the breakage rate depends explicitly on the velocity gradient tensor. In the GCB model, the breakage rate depends on the trace of the conformation tensor associated with species A, being a relative measure for the extension of species A. As stretched micelles are more easily broken apart, we believe that this stress-based criterion is physically more reasonable. Furthermore, Germann et al. [18] showed that the recombination rate must not be a constant as in the VCM model. A similar functional dependence on the microstructural variables associated with species B was derived for the recombination rate. More micellar species can be included in the GCB model in a straightforward manner. In [19, 20], a multi-fluid description was developed to account for standard Fickian diffusion and stress-induced migration. The main feature of the GCB (Germann-Cook-Beris) model is a strong elastic recoil during the start-up of simple shear flow. Although this model has one parameter less than the VCM model under homogeneous flow conditions, it can reliably predict shearing deformations such as steady

simple shear, small-amplitude oscillatory shear, and step strain [18, 19]. The behavior of the GCB model in inhomogeneous extensional flows still needs to be elucidated. Although the VCM and GCB models are both based on Cates's theory, it should be noted that the mechanism of shear band formation is fundamentally different. In these models, shear banding is a consequence of the alignment of the WLMs and their flow-induced breakage. As required by the momentum balance equation, they support the picture of a high shear band with a low viscosity fluid and a low shear band with a highly viscoelastic fluid. Nevertheless, the exact mechanism of shear band formation in entangled threadlike WLMs is still under debate and more experimental research is needed for clarification.

The Giesekus model [21] has been used extensively in the past to examine the rheological and microstructural properties of WLM solutions [2, 22–24]. Fischer and Rehage [22] were the first authors who used this model in the context of WLMs. Because of the nonlinearity of the relaxation term, an overshoot can be generated during a rapid start-up of a simple shearing deformation. In the presence of a sufficiently large solvent contribution, the Giesekus model with a solvent contribution predicts a nonmonotonic flow curve for an anisotropy factor greater than 0.5. The addition of stress diffusion results in the recovery of the monotonic behavior with a small positive slope over the region of shear banding [23]. The Giesekus model shows a good predictability of averaged physical quantities in shearing flows [23, 23, 24]. As it plateaus at high extension rates, it cannot describe the extreme extension thinning behavior as experimentally observed for WLM solutions [25, 26]. The Giesekus model was originally developed for concentrated polymer solutions using kinetic theory [21]. Like many of the standard constitutive models, this model can also be formulated using the generalized bracket approach of nonequilibrium thermodynamics [27]. Although the Giesekus model with diffusion has often successfully been used to represent the steady shear rheology of both rod-like WLMs that exhibit a shear-induced isotropic-nematic transition [23, 23] and entangled threadlike WLMs that shear band due to flow-alignment and disentanglement [28, 29], this model does not include sufficient physics to capture some of the intriguing time-dependent behavior such as observed during start-up of flow [30, 31] and large amplitude oscillatory shear (LAOS) [29].

The goal of this work is to examine the response of the GCB and Giesekus models to Couette flows of steady, start up and LAOS deformations and in doing so, elucidate the role of micellar breakage on the rheological response in the nonlinear regime of steady and dynamic Couette flows. We are comparing predictions of the Giesekus model, which is a one species model that can be considered a nonlinear variant of the Maxwell model to the GCB model, which is a two species model and a nonlinear variant of the VCM model. These two models have the advantage that they are both thermodynamically consistent. Given the significant use of the Giesekus model to in the literature for WLMs, it is important to use it as a reference for building improved models that include more physics of the problem. Importantly, the calculations will be compared against rheological *and microstructural* measurements obtained for a model, entangled threadlike WLM solution cetylpyridinium chloride (CpyCl) surfactant solution in a cylindrical Couette rheometer [28, 29, 31]. The microstructural characteristics including spatiotemporial segmental orientation distributions were simultaneously determined during the rheometric tests using small angle neutron scattering (SANS). The independent determination of local microstructural information within each band and with time resolution provides a unique opportunity to rigorously test constitutive models based on microstructure.

The remainder of the manuscript is as follows. First, the equations of the GCB and Giesekus models are introduced in Secs. 3.1 and 3.2, respectively. In Sec. 3.3, we briefly describe the flow problem and discuss the formulation of the boundary conditions. The calculation of the microstructural characteristics is explained in Sec. 3.4. The experimental protocol is described in Sec. 4. In Sec. 5, the computational results are discussed and compared against the experimental measurements. The final conclusions of this study are drawn in Sec. 6.

3 THEORY

3.1 GCB model

In the GCB model, the WLMs are represented by two species of Hookean dumbbells of molecular weights M_A and $M_B = M_A/2$ and a viscous solvent of molecular weight M_s. Species A represents the longer constituents. One species A is allowed to break in half to form two species B, which can again recombine into one species A. For each species $i = A, B$, we define the number density n_i and the conformation density tensor $\mathbf{C}^i = \mathbf{c}^i n_i$, where $\mathbf{c}$ is the conformation tensor. Here the conformation tensor is defined as the average second moment of the end-to-end connection vector of the microstructural constituents. To reduce the numerical errors in the calculations of inhomogeneous flow, we prefer to use $\mathbf{c}^i$ as unknown rather than $\mathbf{C}^i$. The model is developed upon the basis of the VCM model of Vasquez et al. [16] with the important improvement being the thermodynamically consistent formulation of the breakage and reformation terms.

In the full version of the GCB model [19, 20], a multi-fluid description is employed to account for a direct coupling between flow and concentration. Since no variations in the total micellar concentration could be detected during the experimental tests, we decided to use a simplified version of the GCB model for the comparison. By assuming that all components assume the same velocity, we derive the following time evolution equations:

$$\rho\frac{\partial \mathbf{v}}{\partial t} = -\rho\mathbf{v}\cdot\boldsymbol{\nabla}\mathbf{v} - \boldsymbol{\nabla}p + \boldsymbol{\nabla}\cdot\boldsymbol{\sigma}\,, \tag{1}$$

$$\frac{\partial n_A}{\partial t} = -\boldsymbol{\nabla}\cdot(\mathbf{v}\,n_A) - c_A n_A + \frac{1}{2}c_B n_B^2 + D_A\boldsymbol{\nabla}^2 n_A\,, \tag{2}$$

$$\frac{\partial n_B}{\partial t} = -\boldsymbol{\nabla}\cdot(\mathbf{v}\,n_B) + 2c_A n_A - c_B n_B^2 + D_B\boldsymbol{\nabla}^2 n_B\,, \tag{3}$$

$$\begin{aligned}\frac{\partial \mathbf{c}^A}{\partial t} =& -\mathbf{v}\cdot\boldsymbol{\nabla}\cdot\mathbf{c}^A + \mathbf{c}^A\cdot\boldsymbol{\nabla}\mathbf{v} + (\boldsymbol{\nabla}\mathbf{v})^T\cdot\mathbf{c}^A \\ &- \frac{1}{\lambda_A}\left(\mathbf{c}^A - \frac{k_B T}{K_A}\mathbf{I}\right) + \frac{c_B n_B^2}{n_A}\left(-\frac{1}{2}\mathbf{c}^A + \mathbf{c}^B\right) + D_A\boldsymbol{\nabla}^2\mathbf{c}^A\,,\end{aligned} \tag{4}$$

$$\begin{aligned}\frac{\partial \mathbf{c}^B}{\partial t} =& -\mathbf{v}\cdot\boldsymbol{\nabla}\cdot\mathbf{c}^B + \mathbf{c}^B\cdot\boldsymbol{\nabla}\mathbf{v} + (\boldsymbol{\nabla}\mathbf{v})^T\cdot\mathbf{c}^B \\ &- \frac{1}{\lambda_B}\left(\mathbf{c}^B - \frac{k_B T}{K_B}\mathbf{I}\right) + \frac{c_A n_A}{n_B}\left(\mathbf{c}^A - 2\mathbf{c}^B\right) + D_B\boldsymbol{\nabla}^2\mathbf{c}^B\,.\end{aligned} \tag{5}$$

Equation 1 is the Cauchy momentum balance equation, where ρ is the total mass density of the surfactant solution, p the pressure, $\mathbf{v}$ the velocity, and $\boldsymbol{\sigma}$ the extra stress. The time evolution equations for the number densities of species A and B are given in Eqs. 2 and 3, respectively. The irreversible contributions appearing in Eqs. 3 differ from those appearing in Eqs. 2 only by a negative factor of two because local mass conservation requires the sum $2n_A + n_B$ to be identically constant in the absence of diffusion. In this description of the GBC model, Fickian diffusion has been included to smoothen the profiles. This is in contrast to the more sophisticated two-fluid description that takes into account not only Fickian diffusion but also stress-induced migration. If the initial total micellar concentration is assumed to be uniform as here, then Fickian diffusion does not have an effect on the total micellar concentration [20]. Equations 4 and 5 are the time evolution equations for the conformation tensors $\mathbf{c}^A$ and $\mathbf{c}^B$, respectively, where K_A and $K_B = 2K_A$ are the Hookean spring constants associated with species A and B, respectively, k_B is the Boltzmann constant, and T is the temperature. Together with the left-hand sides, the first three terms on the right-hand sides constitute the upper-convected derivatives of the conformation tensors. The fourth terms on the right-hand sides are Maxwellian relaxation terms. The remaining terms account for the dynamic breakage and reformation processes of the WLMs. It is important to recognize that not only the number densities but also the conformation tensors are affected by these processes.

The deviatoric stress can be calculated using the following explicit expression, which is comprised of the extra stress due to each species plus a solvent term characterized by the solvent viscosity:

$$\boldsymbol{\sigma} = n_A \left(K_A \mathbf{c}^A - k_B T \mathbf{I} \right) + n_B \left(K_B \mathbf{c}^B - k_B T \mathbf{I} \right) + \eta_s \left[\boldsymbol{\nabla} \mathbf{v} + (\boldsymbol{\nabla} \mathbf{v})^T \right] , \tag{6}$$

where η_s is the viscosity of the solvent. The breakage and recombination rates, c_A and c_B, respectively, are given as

$$c_A = c_{Aeq} \exp \left(\frac{\mathrm{tr} \boldsymbol{\sigma}^A}{2 n_A k_B T} \right) \Big/ \sqrt{\det \left(\frac{K_A \mathbf{c}^A}{k_B T} \right)} , \tag{7}$$

$$c_B = c_{Beq} \exp \left(\frac{\mathrm{tr} \boldsymbol{\sigma}^B}{n_B k_B T} \right) \Big/ \det \left(\frac{K_B \mathbf{c}^B}{k_B T} \right) , \tag{8}$$

where c_{Aeq} and c_{Beq} represent the equilibrium breakage and recombination rates, respectively, in the equilibrium state of rest. As can be seen from above, the magnitudes of the nonlinear reaction rates depend on the internal state of the microstructure. For instance, the breakage rate is a scalar function of the trace of the conformation tensor associated with species A. This physical quantity is a measure of the average extension of species A. A similar expression is obtained for the recombination rate. To smooth the transition region between the shear bands, we have added some higher-order derivative diffusive terms to the time evolution equations of the microstructural variables in an ad-hoc fashion. Because of the presence of these terms, the solid boundaries require special consideration. Typically, Neumann conditions are imposed on concentration and conformation/extra stress [32–34]. Alternatively, Dirichlet conditions on the conformation/extra stress can be used. In Bhave et al. [35], the extra stress was determined by requiring the microstructural constituents to be aligned parallel to the boundaries. As a result, their flow curves show a clear nonzero derivative at the boundaries. In this work, we do not impose any additional boundary conditions, thereby making some unnecessary physical assumptions regarding the internal structure of the micelles. Instead, we set the diffusivity equal to zero at the cylindrical walls [20]. Due to local surface effects, diffusion should vanish at these locations within a distance smaller than the radius of gyration. This is because the macromolecules are assumed not to penetrate through the boundaries. Furthermore, they have to take a flat "pancake" conformation to fit next to the rigid walls.

In the equilibrium state of rest ($\mathbf{v} = \mathbf{0}$), we obtain the analytical solution of $n_A = n_A^0$, $n_B = n_B^0 = \sqrt{2 n_A^0 c_{Aeq} / c_{Beq}}$, and $\mathbf{c}^i = (k_B T / K_i)\, \mathbf{I}$ $(i = A, B)$, by taking the linear viscoelastic limit yields as $c_A = c_{Aeq}$ and $c_B = c_{Beq}$.

Under small amplitude oscillatory shear conditions, the storage and loss moduli, G' and G'', respectively, can be approximated as

$$G'(\omega) = G_0 \left\{ \frac{(\lambda_{eff} \omega)^2}{1 + (\lambda_{eff} \omega)^2} + \frac{n_B^0}{n_A^0} \frac{(\lambda_B \omega)^2}{1 + (\lambda_B \omega)^2} \right\} , \tag{9}$$

$$G''(\omega) = G_0 \left\{ \frac{\lambda_{eff} \omega}{1 + (\lambda_{eff} \omega)^2} + \frac{n_B^0}{n_A^0} \frac{\lambda_B \omega}{1 + (\lambda_B \omega)^2} \right\} + \eta_s \omega , \tag{10}$$

where λ_{eff} is the effective relaxation time of the micellar mixture given by [16]

$$\frac{1}{\lambda_{eff}} = \frac{1}{\lambda_A} + c_{Aeq} . \tag{11}$$

Equation 11 shows that the overall relaxation time of the micellar system is reduced from the reptation time due to breakage, which represents another relaxation mechanism of the system. This result is obtained from Cate's theory by just considering two discrete species. If there is no rescaling of the effective relaxation time of the micellar solution from their breakage, we obtain the limiting case $\lambda_{eff} = \lambda_A$. As the contribution from

the solvent viscosity is negligibly small, the upturn of the dynamic moduli arises solely from species B. If the quantities λ_{eff} and $n_B^0/n_A^0 \times \lambda_B$ remain unchanged, then the frequency dependence of the dynamic moduli also remains unchanged. Note that the inverse of the effective relaxation time, $1/\lambda_{eff}$, corresponds to the frequency at which the crossover of the dynamic moduli occurs. The product $n_B^0/n_A^0 \times \lambda_B$ determines the upturn of the loss modulus at high frequencies.

3.2 Giesekus model

Like many other viscoelastic fluid models, the Giesekus model can be formulated using the generalized bracket approach of nonequilibrium thermodynamics [27]. If we formulate the Giesekus model in terms of the conformation tensor, we obtain

$$\boldsymbol{\nabla} \cdot \mathbf{v} = 0\,, \tag{12}$$

$$\rho \frac{\partial \mathbf{v}}{\partial t} = -\rho \mathbf{v} \cdot \boldsymbol{\nabla}\mathbf{v} - \boldsymbol{\nabla} p\,, \tag{13}$$

$$\begin{aligned} \frac{\partial \mathbf{c}}{\partial t} = & -\mathbf{v} \cdot \boldsymbol{\nabla}\mathbf{c} + \mathbf{c} \cdot \boldsymbol{\nabla}\mathbf{v} + (\boldsymbol{\nabla}\mathbf{v})^T \cdot \mathbf{c} \\ & - \frac{1}{\lambda}\left[(1-\alpha)\,\mathbf{I} + \alpha \frac{K}{k_B T}\mathbf{c}\right] \cdot \left(\mathbf{c} - \frac{K}{k_B T}\mathbf{I}\right) + D\boldsymbol{\nabla}^2\mathbf{c}\,, \end{aligned} \tag{14}$$

$$\boldsymbol{\sigma} = G_0 \left(\frac{K}{k_B T}\mathbf{c} - \mathbf{I}\right) + \eta_s \left[\boldsymbol{\nabla}\mathbf{v} + (\boldsymbol{\nabla}\mathbf{v})^T\right]. \tag{15}$$

where λ is the characteristic relaxation time, K the Hookean spring constant, G_0 the modulus of elasticity, and α the anisotropy factor accounting for hydrodynamic interactions. Equations 12 and is 13 are the standard mass and momentum balance equations, respectively. Equation 14 is the time evolution equation for the conformation tensor, $\mathbf{c}$. Together with the left-hand side, the first three terms on the right-hand side constitute the upper-convected derivative of the conformation tensor. The fourth term on the right-hand side of this equation is a nonlinear relaxation term. The last term is a stress diffusive term used to smooth the profiles [23]. The set of time evolution equations 12–14 is closed by an explicit expression for the deviatoric stress provided in Eq. 15, which again includes an explicit solvent contribution. In the presence of a sufficiently large solvent contribution, we obtain an upturn of the loss modulus at high frequencies

Under small amplitude oscillatory shear conditions, the Giesekus model shows the same behavior as the upper-convected Maxwell model. For instance, the storage and loss moduli, G' and G'', respectively, are given by

$$G'(\omega) = \frac{G_0 (\lambda\omega)^2}{1 + (\lambda\omega)^2} \quad \text{and} \quad G''(\omega) = \frac{G_0 (\lambda\omega)}{1 + (\lambda\omega)} + \eta_s \omega\,. \tag{16}$$

3.3 Boundary conditions

To mathematically formulate a cylindrical Couette flow problem, it is convenient to use the cylindrical coordinate system (r, θ, z) as the reference frame, with r, θ, and z being the radial, azimuthal, and axial coordinates, respectively. In all calculations, the inner cylinder with radius R_i was rotated in the clockwise direction whereas the outer cylinder with radius R_o was kept stationary. For simplicity, we neglected any variation in the z-direction. To simulate the start-up of a shear-rate controlled simple shearing deformation, the following condition at the inner cylindrical wall was imposed [5]:

$$v_\theta (r = R_i) = V \tanh(at)\,, \tag{17}$$

where V is the azimuthal velocity at steady state and a is the ramp rate of the rheometer. For narrow gaps, the azimuthal velocity at the inner cylinder can serve as an approximation for the apparent shear rate in the cylindrical gap, i.e. $v_\theta\left(r=R_i\right)/\left(R_o-R_i\right)\approx\dot{\gamma}$. Because it is impossible in practice to achieve an instantaneous jump in the shear rate, we used a hyperbolic tangent function in Eq. 17.

Large oscillatory shear experiments are typically carried out by imposing a sinusoidal deformation at a given magnitude γ_0 and frequency ω. This type of deformation can be simulated by using the following condition for the azimuthal velocity at the inner cylinder [36]:

$$v_\theta\left(R_i\right)=V\cos\left(\omega t\right)\,, \tag{18}$$

where $V=\gamma_0\,\omega\left(R_0-R_i\right)$.

3.4 Microstructural characteristics

To calculate the orientation angle and alignment factor using the predictions by the Giesekus model, we used the formulas provided in [23]. As the GCB model is a two-species model, these formulas had to be adjusted and some averaging had to be done. To calculate the orientation angle of species $i=A,B$, we used the quantity $\mathbf{S}^i$ defined as

$$\mathbf{S}^i=\frac{\mathbf{c}^i}{\mathrm{tr}\mathbf{c}^i}-\frac{1}{3}\mathbf{I}\,. \tag{19}$$

The tensor $\mathbf{S}^i$ describes the deviation of the normalized oriental conformation relative to the quiescent state. The average segmental orientation is the principal eigenvector of $\mathbf{S}^i$, whose projection in the shearing plane gives the average orientation angle

$$\theta^i=\frac{1}{2}\tanh^{-1}\left(-\frac{2\,S^i_{r\theta}}{S^i_{\theta\theta}-S^i_{rr}}\right)\times\frac{180}{\pi}\,. \tag{20}$$

Here an angle of 45° represents a system with orientation along the extension axis of the shear field whereas an angle of 0° represents a system oriented along the shear direction. The average orientation angle of the micelles is obtained by taking into account the concentration of each species (calculated in mass fractions) using the following density-weighted averaging:

$$\theta=\frac{2n_A}{2n_A+n_B}\theta^A+\frac{n_B}{2n_A+n_B}\theta^B\,. \tag{21}$$

The normalized alignment factor A^i_f of species $i=A,B$ is equal the sum of the eigenvalues of $\mathbf{S}^i$ in the shearing plane, such that

$$A^i_f=3\left|S^i_{\theta\theta}+S^i_{rr}\right|\,. \tag{22}$$

A value of $A^i_f=0$ corresponds to an isotropic fluid whereas a value of $A^i_f=1$ represents a perfectly aligned fluid. Thus the alignment factor measures the degree of anisotropy of the fluid relative to the quiescent fluid. To obtain the alignment factor of the micellar mixture, the results were averaged using the same procedure as described above.

$$A_f=\frac{2n_A}{2n_A+n_B}A^A_f+\frac{n_B}{2n_A+n_B}A^B_f\,. \tag{23}$$

4 EXPERIMENTS AND FITTING PROCEDURE

The experimental data reported in this work is for a model, WLM solution comprised of a 6 wt% cetylpyridinium chloride (5.16 wt% of CpyCl monohydrate) /sodium salicylate (1.12 wt%) ([NaSal]/[CPyCl]=0.5) dissolved in 0.5M NaCl D_2O brine. This composition yields a viscoelastic solution that exhibits a nearly Maxwellian equilibrium behavior (with properties listed in Table I) and a threadlike-micellar microstructure that exhibits shear banding [29, 31, 37]. The solutions are formulated in D_2O to enhance SANS contrast and the effects of isotope substitution are known [38]. Also important for comparison to the model predictions are the dimensions of the Coutte cell used in the 1-2 plane SANS measurements ($R_i = 25.5\,\mathrm{mm}$, $R_o = 26.5\,\mathrm{mm}$) [39]. Structure and rheology for steady and transient shear flow [28, 31], LAOS [29, 37] and velocimetry [40, 41] are published and used for comparison in this work. More details and procedures concerning the experiments an their interpretation can be found in the cited works.

The parameters of the GCB and Giesekus models were determined as follows. Small amplitude oscillatory shear data were used to determine the plateau modulus, the effective relaxation time and the product $n_B^0/n_A^0 \times \lambda_B$ associated with the GCB model (see Eqs. 9-10). The equilibrium breakage rate and the normalized quantity n_B^0/n_A^0 were estimated by fitting the GCB model to the steady flow curve in the nonlinear viscoelastic region. The relaxation time, λ_A , of species A was calculated from the effective relaxation time and equilibrium breakage rate using Eq. 11. The values of the product $n_B^0/n_A^0 \times \lambda_B$ and the normalized quantity n_B^0/n_A^0 were used to find the relaxation time, λ_B, of species B. The scaled equilibrium recombination rate $n_A^0 c_{\mathrm{Beq}}$ was determined from the equilibium breakage rate and the normalized quantity n_B^0/n_A^0 using the relationship $n_B^0 = \sqrt{2n_A^0 c_{Aeq}/c_{Beq}}$. For the solvent viscosity appearing in the GCB model, we used the dynamic viscosity of water measured at $25^{\circ}\mathrm{C}$. The plateau modulus and the relaxation time of the Giesekus model were determined by fitting Eq. 16 to small amplitude oscillatory shear data. The anisotropy factor was estimated by fitting the Giesekus model to the steady-state shear stress and first normal stress difference plotted as a function of the shear rate. The solvent viscosity appearing in the Giesekus model was adjusted such that banded velocity profiles are obtained while keeping a good agreement with the shear stress at high shear rates. Consequently, the selected value is almost two orders of magnitude larger than the physical one. A moderate diffusivity was used in both models to smooth the transition region between the shear bands [23]. As in previous works on the VCM model [36, 42, 43] and to better compare with the Giesekus model, where such a distinction cannot be made, we set $D_A = D_B$. The values assigned to the parameters appearing in the equations of the GCB and Giesekus models are provided in Tables 1 and 2, respectively. Inertial effects are not considered in this study. As can be seen from these tables, the plateau modulus of the GCB model is smaller than that of the Giesekus model. We selected a lower plateau modulus for the GCB model to quantitatively capture the stress plateau in the flow curve.

The flow problem was spatially discretized using a Chebyshev polynomials as the base functions [44, 45]. The total number of collocation points corresponded to $N = 200$. For the temporal discretization, a second-order Crank–Nicolson scheme [46] was employed. At every time step, the nonlinear system of discretized algebraic equations was solved using Newton's method [47]. Detailed information about the numerical solution process can be found in [19, 36, 48].

5 RESULTS AND DISCUSSION

5.1 Simple shear flow

In this section, we explore the predictive capability of the GCB and Giesekus models for transient and steady shear-rate controlled simple shear flow. In Figs. 1a and b, we compare the steady-state predictions of the shear stress and first normal stress difference as a function of the shear rate, respectively, against the experimental data. The linear viscoelastic region of the flow curve is well described by the models. The Giesekus model captures the transition between the linear viscoelastic and shear banding regions well. As for the VCM

Table 1: GCB fit parameters and predictions

Parameter	Symbol	Value
Solvent viscosity	η_s	$0.89\,\mathrm{mPa\,s}$
Plateau modulus	G_0	$87\,\mathrm{Pa}$
Relaxation times	λ_A	$0.583\,\mathrm{s}$
	λ_B	$0.002\,\mathrm{s}$
Equilibrium breakage rate	c_{Aeq}	$0.06\,\mathrm{s}^{-1}$
Scaled equilibrium reformation rate	$n_A^0 c_{\mathrm{Beq}}$	$1.6\,\mathrm{s}^{-1}$
Diffusion coefficients	D_A	$2 \times 10^{-9}\,\mathrm{m}^2/\mathrm{s}$
	D_B	$2 \times 10^{-9}\,\mathrm{m}^2/\mathrm{s}$

Table 2: Giesekus fit parameters and predictions

Parameter	Symbol	Value
Solvent viscosity	η_s	$0.09\,\mathrm{Pa\,s}$
Plateau modulus	G_0	$103.2\,\mathrm{Pa}$
Relaxation time	λ	$0.42\,\mathrm{s}$
Anisotropy factor	α	0.74
Diffusion coefficient	D	$2 \times 10^{-9}\,\mathrm{m}^2/\mathrm{s}$

model [43], the GCB model predicts that a stress overshoot before the start of the stress plateau. In this domain of metastability, the transient behavior is very slow and the resulting steady-state velocity profiles are not banded. Although the stress overshoot is not evident in the current measurements, it has been experimentally recorded for a range of nondilute WLM solutions [22, 49, 50]. Furthermore, we find that both models underpredict the shear stress at high shear rates. Also the first normal stress difference is accurately predicted by the models in the linear viscoelastic region. The Giesekus model shows a realistic trend of the first normal stress difference over the whole range of shear rates because of the nonlinear Giesekus relaxation. As will be discussed below, the Giesekus model predicts less strong shear bands, leading to smoother steady-state profiles. Again the GCB model predicts a "kink" followed by a plateau at larger shear rates. The use of a linear Maxwellian Rouse relaxation in Eq. 15 may be the reason why the GCB model fails to capture the shear stress and first normal stress difference at high shear rates, where species B dominates. Improved agreement may be obtained by adopting a nonlinear relaxation mechanism that accounts for micellar stretch.

The kinematic model predictions for steady-state simple shear flow are provided in the left column of Fig. 2, which displays the azimuthal velocity across the cylindrical gap for different shear rates. We observe that the Giesekus model predicts a smoother transition between the bands, which the two-component GCB model shows a sharp "kink" separating the bands, again similar to that reported for the VCM model [43]. If a solvent contribution of the same order of magnitude is included in the partially extended convective (PEC), this model predicts almost the same transition behavior as the VCM model [5]. Therefore, we relate the smooth transition of the Giesekus predictions rather to the nonlinear relaxation term than to the unphysically large solvent contribution. It has been demonstrated for the VCM model that the sharpness of this "kink" broadens with increasing diffusivity, but no adjustments to the diffusivity were studied in this work. Furthermore, we find that the onset of shear banding is moved to higher shear rates. Increasing the magnitude of the shear rate moves the kink separating the shear bands towards the outer stationary cylinder. The location of the kink inside

the cylindrical gap has been plotted as a function of the shear rate in the right column of Fig. 2, showing that the location of the kink is linearly related to the shear rate. This has been confirmed experimentally [31].

Next, we discuss the microstructural characteristics for steady simple shear flow. Fig. 3 displays the concentration of species A across the cylindrical gap predicted by the GCB model for different shear rates. The concentration of species A with respect to the total micellar species, calculated in mass fractions, is given by $\phi^A = 2n_A/(2n_A + n_B)$. The concentration of species B can be estimated from the results displayed in Fig. 3 as the total mass density of the micelles is assumed to be constant in the simplified the GCB model if the diffusion is sufficiently small. This mass constraint has been confirmed by experiments [28]. We find that the concentration of species A is lowest in the high-shear band and highest in the low-shear band, again in agreement with the model predictions of the VCM model [43]. Thus, flow-induced micellar breakage drives the shear banding in the GCB (and VCM) model and the entanglement density will be lower in the higher shear band, as previously deduced from velocimetry measurements [40]. The GCB model predicts that most constituents of species A have been broken near the inner cylinder, i.e., at locations of high deformation. The transition between the two bands is governed by the magnitude of the diffusivity. The larger the value, the less sharp this transition.

A more extensive comparison between microstructural characteristics that were calculated for the GCB model (a-d) and Giesekus model (e-f) and experimental data [31] (solid squares) is provided in Fig. 4. The experimental data displayed in Fig. 4e show that the orientation is close to 45° and is relatively homogeneous across the gap at low shear rates. In the linear viscoelastic region, the orientation angle of the micellar mixture decreases with increasing shear rate, indicating an increased orientation towards the flow. In the shear-banding region, the micelles are highly oriented towards the flow in the high-shear band while the low-shear band has a nearly unaligned microstructure. Furthermore, the experimental results presented in Fig. 4f reveal that the segmental alignment is nearly isotropic and uniform across the gap at low shear rates. In the linear viscoelastic region, the segmental alignment increases with increasing shear rate. In the shear-banding region, the alignment factor is inhomogeneous and increases sharply toward the inner rotating wall. In Figs. 4a and c, we display the orientation angle of the micellar mixture and species A, respectively, calculated for the GBC model as a function of the gap position. The GCB model captures the qualitative behavior of the average orientation angle in the linear viscoelastic region. Nonetheless, it predicts a pronounced undershoot that is not evident in the measurements. However, the orientation angle of species A mimics the correct behavior of the surfactant solution even at large shear rates. The alignment factor of the micellar mixture and species A calculated for the GBC model as a function of the radial position in the cylindrical gap is displayed in Figs. 4b and d, respectively. Again the GCB model predicts the correct trends if only species A is considered. Species B, due to its very fast relaxation time, does not significantly flow align, even in the high shear band region. Therefore, we anticipate that a better quantitative agreement will be obtained if more species are included to better represent the broad distribution of micellar lengths in solution. Interestingly, the Giesekus model can qualitatively describe the spatial dependence of the orientation angle (Fig. 4e) and alignment factor (Fig. 4f) of the micellar mixture, as was reported for other micellar solutions [23]. Furthermore, note that both models fail to properly describe the microstructural characteristics at high shear rates, e.g., a shear rate of $55\,\mathrm{s}^{-1}$. Because they do not properly capture the upturn of the flow curve at high shear rates, they also predict shear band formation outside the experimentally determined shear banding region.

We proceed by discussing the transient behavior of the models. The temporal evolution of the shear stress and first normal stress difference, respectively, are shown in Figs. 5a and b for two different shear rates, $\dot{\gamma} = 2.2\,\mathrm{s}^{-1}$ and $22\,\mathrm{s}^{-1}$. Both models can qualitatively predict for the overshoot of the shear stress occurring during the start-up of the nonlinear deformation, but only the GCB model can capture the abruptness of the drop in stress after the extremum. This is because the models differ fundamentally in the molecular mechanisms that produce this overshoot: Whereas the GCB model uses flow-induced micellar breakage, the Giesekus model uses a nonlinear type of relaxation. A prior report for startup of shear for the VCM model show a similar stress overshoot and a similar, abrupt drop in stress as well [43]. The conclusion that the abruptness of the drop is related to the flow-induced breakage of the WLMs will have to be experimentally verified. However, we believe

that this explanation is reasonable as the breakage rate appearing in the GCB model depends on the trace of the conformation tensor, being a relative measure of the extension of the longer species. During the start-up of simple shear flow, the micelles are stretched until they are forced to break apart. Very recently, Germann et al. [20] showed that the full version of the GCB model, which accounts for a direct coupling between flow and concentration, can more realistically describe the sigmoidal decay of the shear stress. Finally, note that the GCB model exhibits a few damped oscillations after the stress overshoot, as experimentally verified for various WLM solutions [11, 12]. As already pointed out above, the Giesekus model can better capture the first normal stress difference.

The temporal evolution of the azimuthal velocity in the cylindrical gap is plotted in Fig. 6 for $\dot{\gamma} = 22\,\mathrm{s}^{-1}$. At small times, the GCB model (left figure) predicts an increase of the azimuthal velocity at the inner wall. After the occurrence of the stress maximum, the fluid undergoes an elastic recoil resulting in a local minimum of the azimuthal velocity near the inner cylinder. The GCB model predicts a (transient) negative minimum velocity because of the high nonlinearity of the breakage rate. Essentially, the flow-induced breakage of species A in the faster moving fluid region leads to a temporary elastic recoil of the highly viscolastic fluid rich in species A that is flowing slowly. A similar retrograde response is observed for the VCM model as well [43]. Afterwards, the velocity forms a profile with two distinct bands and undergoes a few damped oscillations to recover from the strong elastic recoil. Finally, stress diffusion pushes this profile towards the inner cylinder. The Giesekus model predicts a similar start up (right figure), but because this model only predicts a weak elastic recoil, the azimuthal velocity does not become negative. To better explore this behavior, the temporal evolution of the azimuthal velocity evaluated at two different radial positions, $(r - R_i) \,/\, (R_o - R_i) = 0.2$ and 0.8, is displayed in Fig. 7. As expected, under conditions near to the linear viscoelastic regime (Fig. 7a), both models predict that the azimuthal velocity increases smoothly until it reaches a steady state. The magnitude of the azimuthal velocity is higher near the inner cylinder because of the greater deformation. For $\dot{\gamma} = 22\,\mathrm{s}^{-1}$ (Fig. 7b), the GCB model (solid lines) predicts a sudden decrease because of the pronounced breakage of the micelles. Only a weak recoil has been experimentally observed in controlled shear-rate experiments for WLMs [51, 52]. However, by accounting for nonlinear relaxation, we believe that the recoil can be mitigated. Finally, the evolution of the velocity at these positions predicted by the Giesekus model (dashed lines) is smoother and more realistic.

The temporal evolution of the microstructural characteristics at the inner cylindrical wall are shown in Figs. 8 and 9for $\dot{\gamma} = 2.2\,\mathrm{s}^{-1}$ and $\dot{\gamma} = 22\,\mathrm{s}^{-1}$, respectively. Under linear viscoelastic conditions, the Giesekus model (dashed lines) quantitatively predicts the average orientation angle and alignment factor displayed in Figs. 8a and b, respectively. Whereas the GCB model (solid lines) excellently captures the average orientation angle, it greatly overpredicts the average alignment factor. The concentration of species A calculated for the GCB model is displayed in Fig. 8c. As expected, the concentration of species A decreases with time until it assumes a steady state. As soon as the cylinder starts to rotate, the flow enhances the breakage of the longer micelles. As the Giesekus model cannot describe the abrupt drop in shear stress during the start-up of a nonlinear deformation, the predictive capability of the Giesekus model is worse for $\dot{\gamma} = 22\,\mathrm{s}^{-1}$. We find that the Giesekus model can qualitatively describe the overall transient behavior, but it fails to exactly capture the microstructural changes during the stress release. The agreement between the experimental data and the GCB model is also not satisfactory. As species B does not significantly flow align in the high shear rate band, the GCB model cannot quantitatively capture the experimental data. More species will have to be included in the GCB model to more realistically represent the distribution of micellar lengths in solution.

5.2 Large Amplitude Oscillatory Shear

In this section, we assess the *predictive* capability of the GCB and Giesekus models for large amplitude oscillatory shear under conditions of homogeneous flow kinematics as well as conditions for which dynamic shear banding is observed. We start with the elastic Lissajous-Bowditch diagrams displayed in Fig. 10. The numerical data displayed in these diagrams were collected after 8 oscillatory cycles to assure that the initial transients have been sufficiently decayed. At a relatively small value of strain and a moderate angular frequency, the

predictions of both models agree with the experimental results (see Fig. 10a). We believe that the success of the Giesekus model is because the model includes a nonlinear relaxation. We find that the GCB model (solid lines) overpredicts the magnitude of the shear stress. Under this flow condition, no shear banding occurs. If the strain is doubled while keeping the angular frequency constant, the stress signal is a little tilted forward with a sinusoidal shape, and the Lissajous pattern is distorted from an ellipse (see Fig. 10b). Again the GCB model overpredicts the experimental trends. Nevertheless, it accounts for the change of shape, which may experimentally be related to the shear band formation of the material. In the GCB model, the stress overshoot is caused by the flow-induced breakage. Subsequently, shear bands are formed. This is because a model with a non-monotonic homogeneous constitutive curve that admits steady-state banding is expected to exhibit shear banding at small frequencies and sufficiently high strain rates, as the shear rate quasi-statically transits the plateau in the steady flow curve. The Lissajous curve calculated for the Giesekus model (dashed lines) assumes a parallelogram-like shape without a stress overshoot. The predictions of the GCB and Giesekus models significantly deviate from the experimental data as the angular frequency is further increased at this high strain value (see Fig. 10c). The disagreement between experiment and the models may be related to the fact that the models do not account for shear-induced demixing observed near the high transient stresses (for a discussion, see [29]). We also note that the GCB model predicts a much sharper overshoot in stress than the data and the Giesekus model under these conditions. In summary, the Giesekus model is capable of quantitatively capturing the experimental trends at small frequencies and strains because of the nonlinear relaxation. If the strain is further increased, the GCB model outperforms the Giesekus model. This may be because the flow-induced breakage induces more pronounced shear bands in the GCB model. At high frequencies, both models fail because they do not take into account the effect of shear-induced demixing.

The azimuthal velocity across the cylindrical gap is plotted in Fig. 11, where the velocity is calculated at the instant when the wall velocity is maximum, minimum, zero and increasing, and zero and decreasing. The calculations were made for a strain of $\gamma_0 = 10$ and two different values of the angular frequency, namely $\omega = 0.56\,\mathrm{rad/s}$ (left column), and $\omega = 5.6\,\mathrm{rad/s}$ (right column). We find that the GCB model (top row) predicts banded profiles for both conditions. For the smaller angular frequency, the location of the kink is closer to the inner wall. Also the absolute value of the azimuthal velocity at the location of the kink is higher. Interestingly, no banding can be observed in the profiles calculated for the Giesekus model (bottom row). A detailed study of LAOS flows of the VCM model by Zhou et al. [36] shows qualitative characteristics for the transient shear stress and velocity profile for comparable values of Deborah and Weissenberg numbers. Strongly banded velocity profiles during LAOS and stress overshoots during the oscillatory cycle were obtained as a consequence of the flow-induced breakage of species A. In the same study, they assembled the computational results into a Pipkin diagram defining the parameter space where shear banding is predicted by the VCM model.

The concentration of species A is plotted in Fig. 12 for the GCB model at two different radial positions, $(r - R_i) / (R_o - R_i) = 0.2$ and 0.8 for one oscillation cycle in the alternance state. The system was periodically deformed using a strain of $\gamma_0 = 10$ and angular frequencies of $\omega = 0.56\,\mathrm{rad/s}$ (left column) and $\omega = 5.6\,\mathrm{rad/s}$ (right column). In both cases, obtain a rapid decrease in species A concentration is observed during the elastic recoil. This phenomenon, however, is more pronounced for $\omega = 5.6\,\mathrm{rad/s}$. Moreover, we find that increasing the angular frequency increases the difference in species A concentration across the cylindrical gap as the system exhibits shear banding.

The temporal evolution of the average orientation angle and alignment factor over one cycle is displayed in the left and right columns of Fig. 13, respectively, for $\omega = 0.56\,\mathrm{rad/s}$ and $\gamma_0 = 5$. We observe that the GCB model (sold lines) captures the experimental trends, but greatly overpredicts the alignment factor. The influence of the radial position on the alignment factor is not pronounced, confirming that a nearly homogeneous shear flow is present as expected for this condition. The Giesekus model (dashed lines) predicts qualitatively the same trends. The corresponding results for a strain of $\gamma_0 = 10$ and two different values of the angular frequency, namely $\omega = 0.56\,\mathrm{rad/s}$ and $\omega = 5.6\,\mathrm{rad/s}$, are shown in Fig. 14 and Fig. 15, respectively. We find that the GCB model (solid lines) predicts sharp unphysical changes in the orientation angle (left column) and alignment factor (right column) as a result of the strong elastic recoil. Overall, the predictions of the GCB model are

satisfactory and may be further improved by adding more species. Interestingly, the Giesekus model greatly overpredicts the alignment angle displayed in Fig. 15c. Overall, the qualitative behavior of the Giesekus model (dashed lines) is satisfactory.

Several experimental works have indicated the importance of dynamic breakage in the micellar solution rheology. Although the fast breaking limit leads to Maxwellian-like behavior for the linear viscoelastic properties, equilibrium micellar breakage and reptation times can be widely separated, such as for the threadlike micelle solutions studied here. Cates and Candau [9] and recent work by Zou et al. [15] show that accounting for micellar breakage is necessary to fully explain the linear viscoelasticity of such systems. In the fast breaking limit, the reaction dynamics lead to a single relaxation time, which is manifested as a semi-circle in the Cole-Cole representation. Work by Sachsenheimer et al. [53] demonstrates the importance of micellar breakage in the elongational rheology of WLM solutions. Micellar breakage is clearly evident in the dramatic release of stress upon nonlinear flow start up [31] and more recently, has been implicated in explaining the highly nonlinear shear banding behavior of branched WLMs [7]. The current predictions of the GCB model reveal that flow-induced breakage can have a tremendous impact on the nonlinear rheology. More experimental research is needed to clarify the role of flow-induced breakage in the process of the shear band formation in entangled threadlike WLMs, where evidence for the change in average micelle contour length in the flow would be valuable.

In this study, we found that the Giesekus model predicts some averaged physical quantities more reliably than the GCB model, while the GCB model can better capture the disparate timescales evident in the dynamic measurements and the shear banding observed in experiments. Because of these reasonable predictions by the Giesekus model, we believe that the GCB model can further be improved by accounting for nonlinear relaxation or a direct coupling of the relaxation modes [54]. As demonstrated in Germann et al. [18], the GCB model can describe the qualitative trends of SAOS data. The severe discrepancy between the microstructural measurements and the predictions of the GCB model are also due to the fact that species B, which has an extremely fast relaxation time relative to that of species A, does not flow align under the conditions of these experiments. If the relaxation behavior of WLMs is similar to that of polymer melts, one would expect the reptational relaxation to scale as $\lambda_A \sim (L/L_E)^3$ and the Rouse-like relaxation time to scale as $\lambda_B \sim (L/2L_E)^2$ [55]. Here L, $L/2$ respectively, is the micellar length in the equilibrium state of rest and and L_E is the micellar entanglement length. Hence, we should then get the scaling relation $\lambda_B/\lambda_A \sim L_E/4L$. The values obtained for this ratio by fitting the GCB model with the experimental data, however, was of much smaller magnitude. A more realistic description could be obtained by incorporating intermediate species, which can be accomplished in a straightforward fashion [18].

6 CONCLUSIONS

In this study, we evaluate the capability of two thermodynamically consistent constitutive models to predict the rheological and microstructural characteristics of a model viscoelastic WLM surfactant solution undergoing simple shear and large amplitude oscillatory shear in a cylindrical Couette rheometer. The first model is a new, two-species model (based on the VCM model) specifically developed for WLMs that includes flow-induced micellar breakage, whereas the second model is the Giesekus model with solvent and diffusion that is based on one component (nonbreaking) with nonlinear relaxation. The microstructure of the micellar solution was simultaneously measured using spatio-temporally resolved small angle neutron scattering in the plane of flow, providing a much more rigorous test of the structure-property relationships underlying the model.

We find that both models can capture many of the qualitative trends observed for transient and steady simple shear data in the linear viscoelastic and shear-banding regimes. Quantitative differences between the GCB model and the experimental data are observed at large shear rates, and the nonlinear micellar breakage mechanism in the GCB model leads to a significant mechanism for rapid stress relaxation, such as observed in nonlinear shear start-up experiments and LAOS flows. To quantitatively capture these trends, however, we believe that it will be necessary to account for nonlinear relaxation behavior and intermediate micellar species.

More experimental research is needed to determine the role of flow-induced breakage in the nonlinear rheology of WLM solutions. Furthermore, we find that both models can semi-quantitatively predict LAOS flows if the applied angular frequency is not too high. However, flow-induced micellar breakage leads to predictions of sharp, well defined shear bands and stress overshoots during the LAOS cycle for the GCB model, as was also reported for the VCM model. Finally, to obtain a better quantitative agreement at high angular frequencies, it may be necessary to account for the shear-induced demixing observed in experiments.

The results of this study confirm that the Giesekus model can reasonably predict many of the mass-averaged rheological and microstructural characteristics of WLM solutions in shearing flows. Because of the nonlinear type of relaxation, the Giesekus model can capture the steady normal stress data even at large shear rates. As opposed to the GCB model, the Giesekus model predicts a weak elastic recoil. Therefore, the local minimum of the azimuthal velocity formed as a result of the elastic recoil did not change sign. It remains to be experimentally assessed in the future whether this prediction is reasonable. A major limitation of the Giesekus model is that an unphysically large solvent contribution is required to capture the shear stress at large shear rates. Furthermore, it does not account for the flow-induced breakage and recombination events, and as such cannot capture the characteristics in strong flows. Also because of this limitation, the Giesekus model cannot describe the extreme extension thinning behavior of WLM solutions. This work further supports the importance of explicitly including breakage in rheological constitutive models for WLM solutions, and demonstrates the value of including microstructural information along with bulk rheology and flow velocimetry in resolving and testing constitutive models.

References

[1] P. D. Olmsted, O. Radulescu, and C. Y. D. Lu. Johnson–Segalman model with a diffusion term in cylindrical couette flow. *J. Rheol.*, 44(2):257–275, 2000.

[2] M. E. Helgeson, P. A. Vasquez, E. W. Kaler, and N. J. Wagner. Rheology and spatially resolved structure of cetyltrimethylammonium bromide wormlike micelles through the shear banding transition. *J. Rheol.*, 53(3):727–756, 2009b.

[3] R. G. Larson. A constitutive equation for polymer melts based on partially extending strand convection. *J. Rheol.*, 28(5):545–571, 1984.

[4] A. E. Likhtman and R. S. Graham. Simple constitutive equation for linear polymer melts derived from molecular theory: Rolie–poly equation. *J. Non-Newt. Fluid Mech.*, 114(1):1–12, 2003.

[5] L. Zhou, P. A. Vasquez, L. P. Cook, and G. H. McKinley. Modeling the inhomogeneous response and formation of shear bands in steady and transient flows of entangled liquids. *J. Rheol.*, 52(2):591–623, 2008.

[6] M. A. Fardin, D. Lopez, J. Croso, G. Grégoire, O. Cardoso, G. H. McKinley, and S. Lerouge. Elastic turbulence in shear banding wormlike micelles. *Phys. Rev. Lett.*, 104:178303, 2010.

[7] M. A. Calabrese, S. A. Rogers, R. P. Murphy, and N. J. Wagner. The rheology and microstructure of branched micelles under shear. *J. Rheol.*, 59:1299, 2015.

[8] M. E. Cates. Reptation of living polymers: dynamics of entangled polymers in the presence of reversible chain-scission reactions. *Macromolecules*, 20(9):2289–2296, 1987.

[9] M. E. Cates and S. J. Candau. Statics and dynamics of worm-like surfactant micelles. *Journal of Physics: Condensed Matter*, 2(33):6869–6892, 1990.

[10] N. A. Spenley, M. E. Cates, and T. C. B. McLeish. Nonlinear rheology of wormlike micelles. *Phys. Rev. Lett.*, 71:939–942, 1993.

[11] J.-F. Berret. Transient rheology of wormlike micelles. *Langmuir*, 13(8):2227–2234, 1997.

[12] S. Lerouge, J.-P. Decruppe, and J.-F. Berret. Correlations between rheological and optical properties of a micellar solution under shear banding flow. *Langmuir*, 16(16):6464–6474, 2000.

[13] M.-A. Fardin and S. Lerouge. Flows of living polymer fluids. *Soft Matter*, 10:8789–8799, 2014.

[14] W. Zou and R. G. Larson. A mesoscopic simulation method for predicting the rheology of semi-dilute wormlike micellar solutions. *J. Rheol.*, 58(3):681–721, 2014.

[15] W. Zou, X. Tang, M. Weaver, P. Koenig, and R. G. Larson. Determination of characteristic lengths and times for wormlike micelle solutions from rheology using a mesoscopic simulation method. *J. Rheol.*, 59 (4):903–934, 2015.

[16] P. A. Vasquez, G. H. McKinley, and L. P. Cook. A network scission model for wormlike micellar solutions: I. model formulation and viscometric flow predictions. *J. Non.-Newt. Fluid Mech.*, 144(2–3):122 –139, 2007.

[17] M. Grmela, F. Chinesta, and A. Ammar. Mesoscopic tube model of fluids composed of worm-like micelles. *Rheol. Acta*, 49:495–506, 2010.

[18] N. Germann, L. P. Cook, and A. N. Beris. Nonequilibrium thermodynamic modeling of the structure and rheology of concentrated wormlike micellar solutions. *J. Non-Newt. Fluid Mech.*, 196:51–57, 2013.

[19] N. Germann, L. P. Cook, and A. N. Beris. Investigation of the inhomogeneous shear flow of a wormlike micellar solution using a thermodynamically consistent model. *J. Non-Newt. Fluid Mech.*, 207:21–31, 2014.

[20] N. Germann, L. P. Cook, and A. N. Beris. A differential velocities-based study of diffusion effects in shear-banding micellar solutions. *J. Non-Newt. Fluid Mech.*, 232:43–54, 2016.

[21] H. Giesekus. A simple constitutive equation for polymer fluids based on the concept of the deformation dependent tensorial mobility. *J. Non-Newt. Fluid Mech.*, 11(1–2):69–109, 1982.

[22] P. Fischer and H. Rehage. Non-linear flow properties of viscoelastic surfactant solutions. *Rheol. Acta*, 36 (1):13–27, 1997.

[23] M. E. Helgeson, M. D. Reichert, Y. T. Hu, and N. J. Wagner. Relating shear banding, structure, and phase behavior in wormlike micellar solutions. *Soft Matter*, 5(20):3858–3869, 2009a.

[24] M. W. Liberatore, F. Nettesheim, P. A. Vasquez, M. E. Helgeson, N. J. Wagner, E. W. Kaler, L. P. Cook, L. Porcar, and Y. T. Hu. Microstructure and shear rheology of entangled wormlike micelles in solution. *J. Rheol.*, 53(2):441–458, 2009.

[25] R. K. Prud'homme and G. G. Warr. Elongational flow of solutions of rodlike micelles. *Langmuir*, 10(10): 3419–3426, 1994.

[26] L. M. Walker, P. Moldenaers, and J.-F. Berret. Macroscopic response of wormlike micelles to elongational flow. *Langmuir*, 12(26):6309–6314, 1996.

[27] A. N. Beris and B. J. Edwards. *Thermodynamics of Flowing Systems*. Oxford University Press, New York, 1994.

[28] A. K. Gurnon, C. Lopez-Barron, M. J. Wasbrough, L. Porcar, and N. J. Wagner. Spatially resolved concentration and segmental flow alignment in a shear-banding solution of polymer-like micelles. *ACS Macro Letters*, 3(3):276–280, 2014.

[29] A. K. Gurnon, C. R. Lopez-Barron, A. P. R Eberle, L. Porcar, and N. J. Wagner. Spatiotemporal stress and structure evolution in dynamically sheared polymer-like micellar solutions. *Soft Matter*, 10(16):2889–2898, 2014a.

[30] Y. T. Hu and A. Lips. Kinetics and mechanism of shear banding in an entangled micellar solution. *J. Rheol.*, 49:1001, September 2005.

[31] C. R. Lopez-Barron, A. K. Gurnon, A. P. R. Eberle, L. Porcar, and N. J. Wagner. Microstructural evolution of a model, shear-banding micellar solution during shear start-up and cessation. *Phys. Rev. E*, 89(4): 042301, 2014.

[32] V. G. Mavrantzas, A. Souvaliotis, and A. N. Beris. Pseudospectral calculations of stress-induced concentration changes in viscometric flows of polymer solutions. *Theoret. Comput. Fluid Dynamics*, 5(1):3–31, 1993.

[33] L. P. Cook and L. F. Rossi. Slippage and migration in models of dilute wormlike micellar solutions and polymeric fluids. *J. Non-Newt. Fluid Mech.*, 116(2–3):347–369, 2004.

[34] W. B. Black and M. D. Graham. Slip, concentration fluctuations, and flow instability in sheared polymer solutions. *Macromolecules*, 34(17):5731–5733, 2001.

[35] A. V. Bhave, R. C. Armstrong, and R. Brown. Kinetic theory and rheology of dilute, nonhomogeneous polymer solutions. *J. Chem. Phys.*, 95(4):2988–3000, 1991.

[36] L. Zhou, L. P. Cook, and G. H. McKinley. Probing shear-banding transitions of the VCM model for entangled wormlike micellar solutions using large amplitude oscillatory shear (LAOS) deformations. *J. Non-Newt. Mech.*, 165(21–22):1462–1472, 2010.

[37] A. K. Gurnon and N. J. Wagner. Large amplitude oscillatory shear (LAOS) measurements to obtain constitutive equation model parameters: Giesekus model of banding and nonbanding wormlike micelles. *J. Rheol.*, 56(2):333–351, 2012. doi: 10.1122/1.3684751.

[38] C. R. Lopez-Barron and N. J. Wagner. Solvent isotope effect on the microstructure and rheology of cationic worm-like micelles near the isotropic-nematic transition. *Soft Matter*, 22(7):10856–10863, 2011.

[39] A. K. Gurnon, P. D. Godfrin, N. J. Wagner, A. P. R. Eberle, P. Butler, and L. Porcar. Measuring material microstructure under flow using 1-2 plane flow-small angle neutron scattering. *JoVE*, 84:e51068, 2014.

[40] Y. T. Hu and A. Lips. Kinetics and mechanism of shear banding in an entangled micellar solution. *J. Rheol.*, 49(5):1001–1027, 2005.

[41] Y. T. Hu, C. Palla, and A. Lips. Comparison between shear banding and shear thinning in entangled micellar solutions. *J. Rheol.*, 52(2):379–400, 2008.

[42] L. Zhou, L. P. Cook, and G. H. McKinley. Multiple shear-banding transitions for a model of wormlike micellar solutions. *SIAM Appl. Math.*, 72(4):1192–1212, 2012.

[43] L. Zhou, L. P. Cook, and G. H. McKinley. Wormlike micellar solutions: III. VCM model predictions in steady and transient shearing flows. *J. Non-Newt. Mech.*, 211:70–83, 2014.

[44] D. Gottlieb, M. Y. Hussaini, and S. A. Orszag. Theory and application of spectral methods. In *Spectral Methods for Partial Differential Equations*, pages 1–54. SIAM Press, Philadelphia, 1984.

[45] R. Peyret. *Spectral Methods for Incompressible Viscous Flow*. Springer-Verlag, New York, 2002.

[46] R. D. Richtmeyer and K. W. Morton. *Difference Methods for Initial-Value Problems*. Interscience, New York, 1967.

[47] J. E. Dennis and R. B. Schnabel. *Numerical Methods for Unconstrained Optimization and Nonlinear Equations*. Prentice-Hall Press, Englewood Cliffs, 1983.

[48] N. Germann, M. Dressler, and E. J. Windhab. Numerical solution of an extended White-Metzner model for eccentric Taylor-Couette flow. *J. Comp. Phys.*, 230(21):7853–7866, 2011.

[49] C. Grand, J. Arrault, and M. E. Cates. Slow transients and metastability in wormlike micelle rheology. *J.Phys. II*, 7(1):1071–1086, 1997.

[50] A.vF. Méndez-Sánchez, M. R. López-González, V. H. Rolón-Garrido, J. Pérez-González, and L. de Vargas. Instabilities of micellar systems under homogeneous and non-homogeneous flow conditions. *Rheol. Acta*, 42(1–2):56–63, 2003.

[51] P. E. Boukany and S. Q. Wang. Use of particle-tracking velocimetry and flow birefringence to study nonlinear flow behavior of entangled wormlike micellar solution: from wall slip, bulk disentanglement to chain scission. *Macromol.*, 41(4):1455–1464, 2008.

[52] M. Ouchi, T. Takahashi, and M. Shirakashi. Shear-induced structure change and flow-instability in start-up Couette flow of aqueous, wormlike micelle solution. *J. Rheol.*, 50(3):341–352, 2006.

[53] D. Sachsenheimer, C. Oelschlaeger, S. Müller, J. Küstner, S. Bindgen, and N. Willenbacher. Elongational deformation of wormlike micellar solutions. *J. Rheol.*, 58(6):2017–2042, 2014.

[54] B. J. Edwards, A. N. Beris, and V. G. Mavrantzas. A model with two coupled Maxwell modes. *J. Rheol.*, 40(5):917–942, 1996.

[55] M. E. Cates. Flow behaviour of entangled surfactant micelles. *J. Phys.: Condens. Matter*, 8(47):9167–9176, 1996.

7 ACKNOWLEDGEMENTS

We acknowledge the support of the National Institute of Standards and Technology, U.S. Department of Commerce, and the Institut Laue-Langevin in Grenoble, France in providing the neutron research facilities used in this work. This manuscript was prepared under cooperative agreement 70NANB12H239 from NIST, U.S. Department of Commerce. The statements, findings, conclusions and recommendations are those of the author(s) and do not necessarily reflect the view of NIST or the U.S. Department of Commerce.

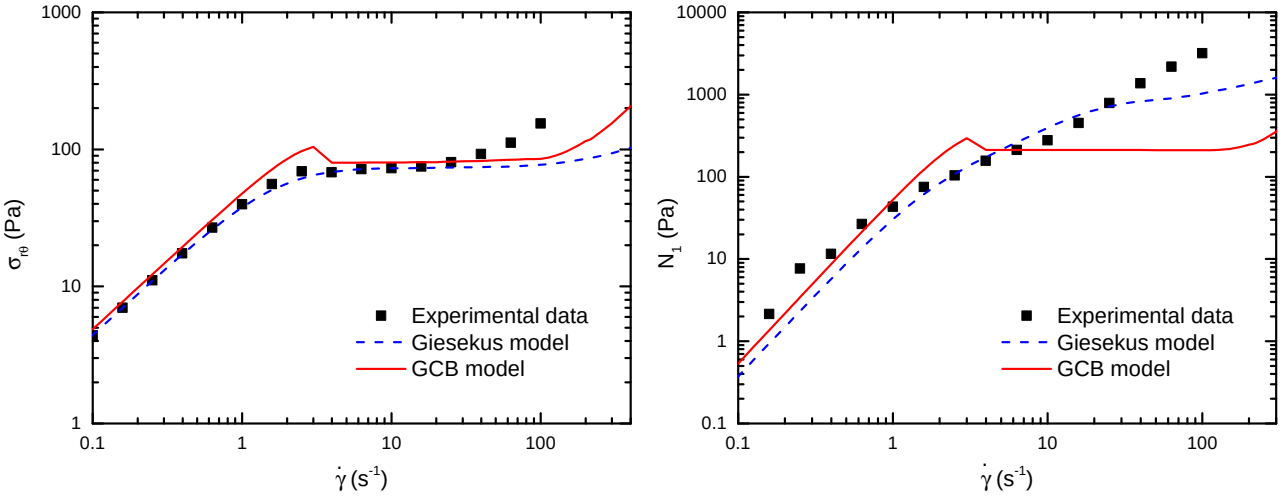

Figure 1: Validation of models with experimental data obtained for steady-state simple shear flow. Shear stress (left column) and first normal stress difference (right column) as a function of the shear rate.

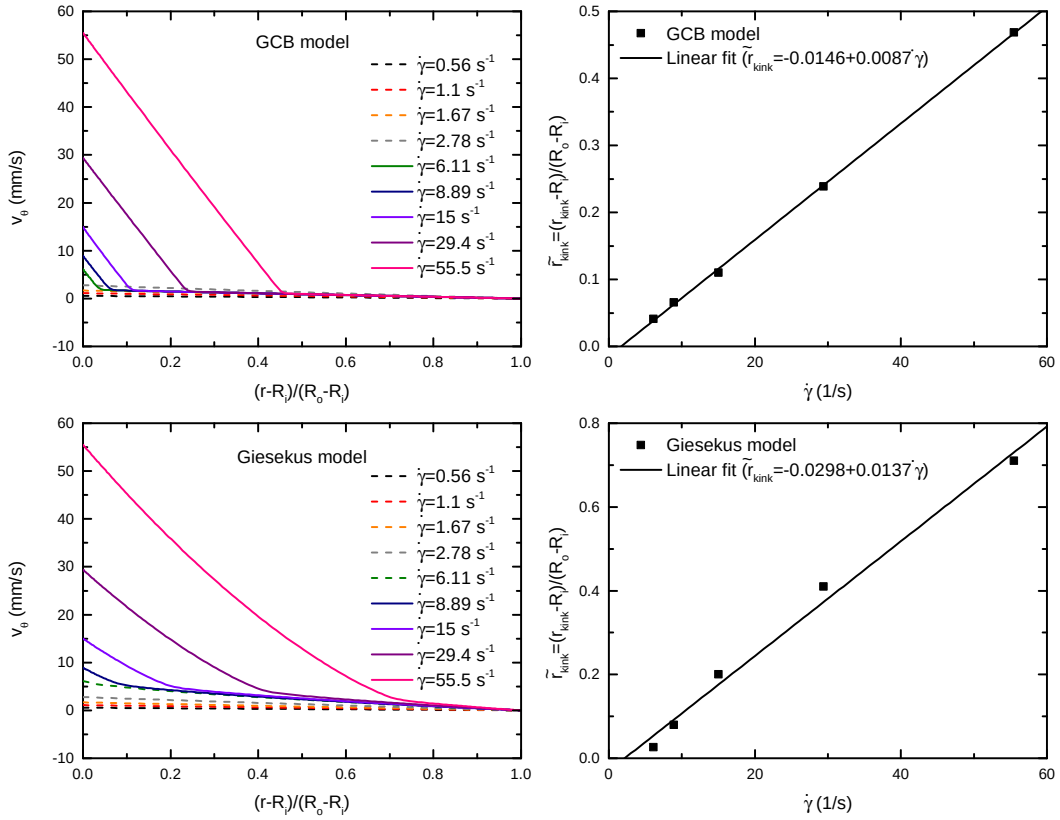

Figure 2: Kinematic characteristics predicted by GCB model (top row) and Giesekus model (bottom row) for steady-state simple shear flow. Left column: azimuthal velocity across cylindrical gap calculated for different shear rates. Right column: position of kink as a function of the shear rate. The numerical results (rectangles) were fitted using a linear function (solid line).

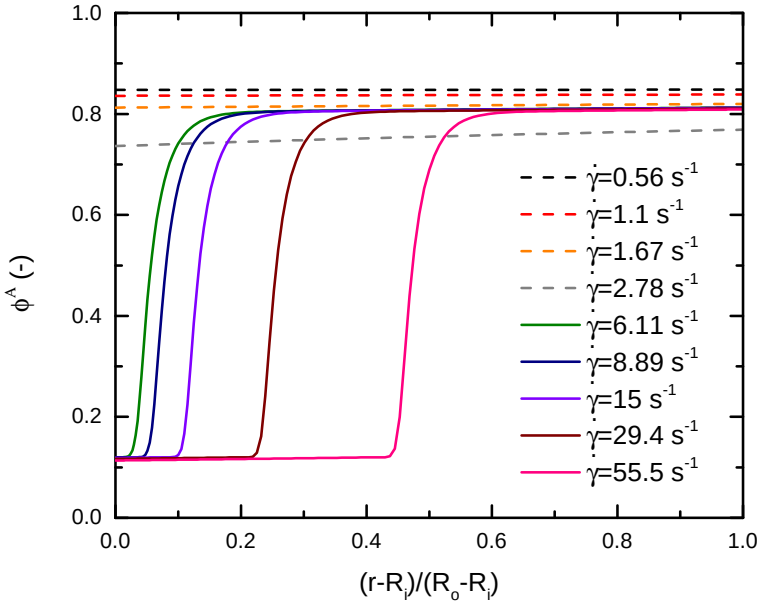

Figure 3: Concentration in mass fractions of species A across cylindrical gap predicted by GCB model for different shear rates.

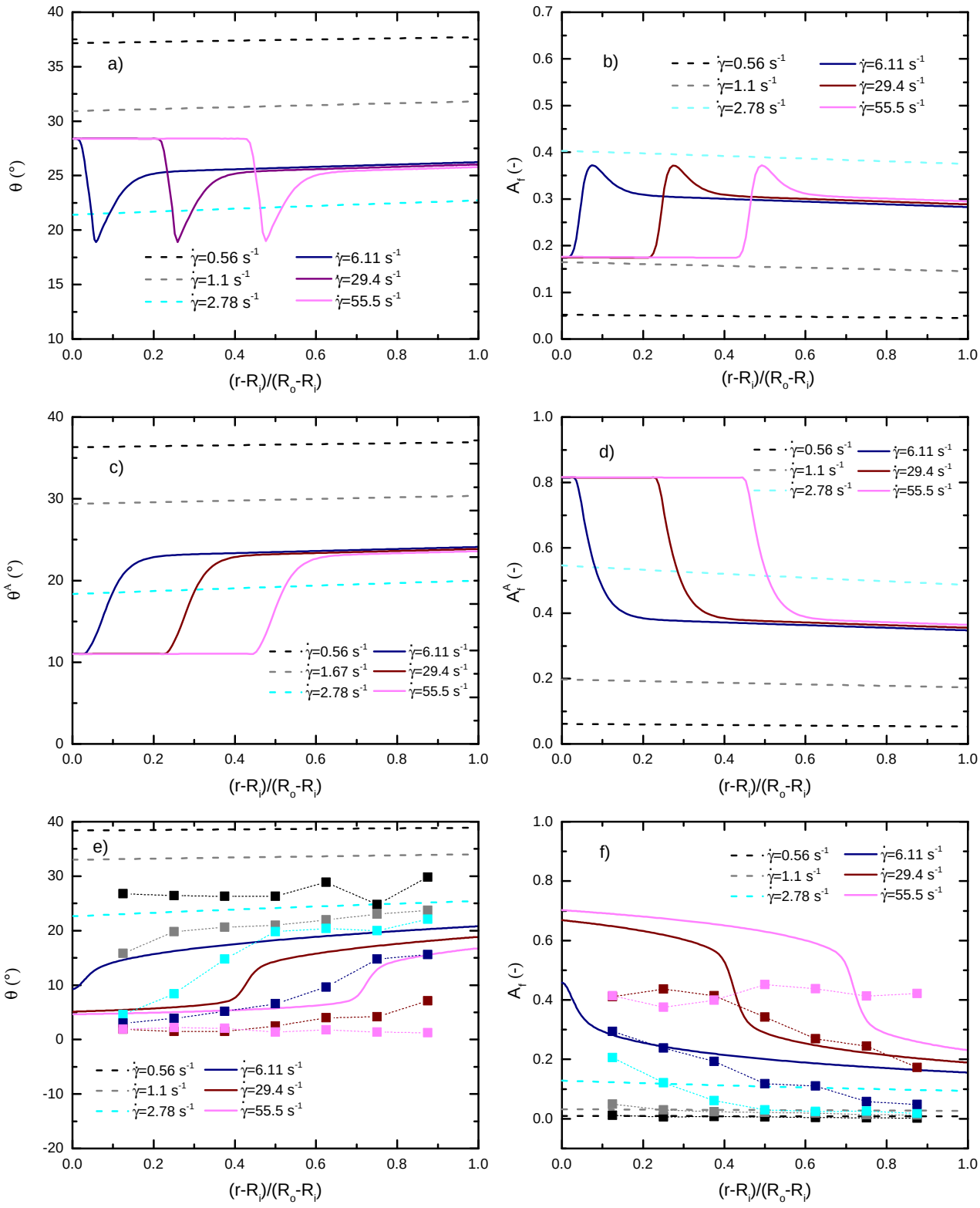

Figure 4: Microstructural characteristics across cylindrical gap predicted by GCB model (a-d) and Giesekus model (e and f) for different shear rates. a) and e) Orientation angle of mixture, b) and f) alignment factor of mixture, c) orientation angle of species A, and d) alignment factor of species A versus radial position in cylindrical gap.

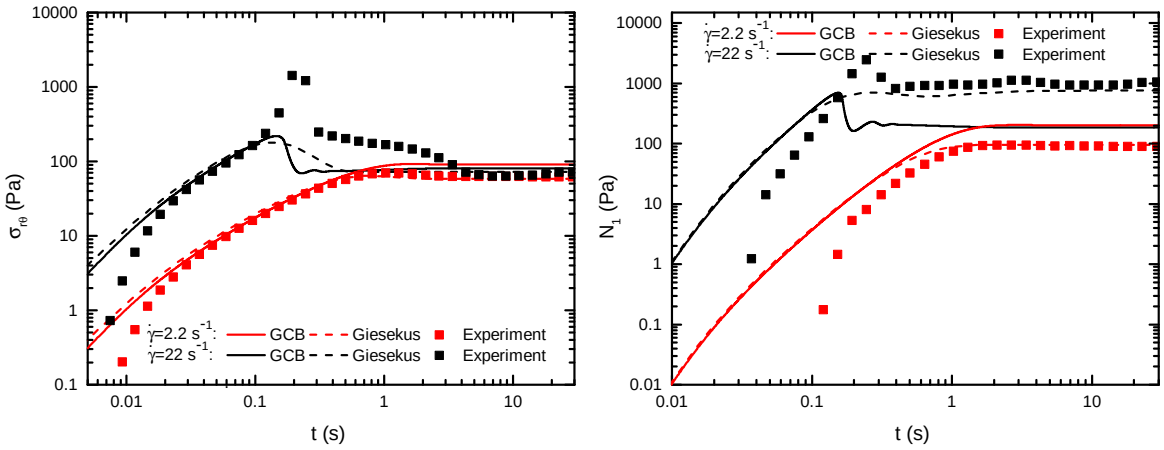

Figure 5: Temporal evolution of shear stress (left column) and first normal stress difference (right column) predicted by GCB model (solid lines) and Giesekus model (dashed lines) for two different shear rates at inner cylindrical wall. A ramp-up rate of $a = 110\,\mathrm{s}^{-1}$ was used.

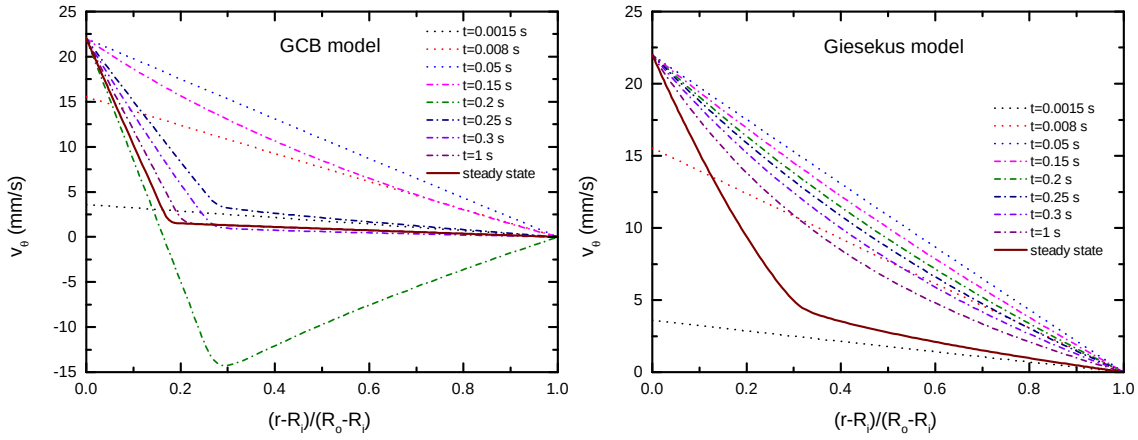

Figure 6: Temporal evolution of azimuthal velocity across cylindrical gap during start-up of simple shear flow ($\dot{\gamma} = 22\,\mathrm{s}^{-1}$) calculated for GCB model (left column) and the Giesekus model (right column). A ramp-up rate of $a = 110\,\mathrm{s}^{-1}$ was used.

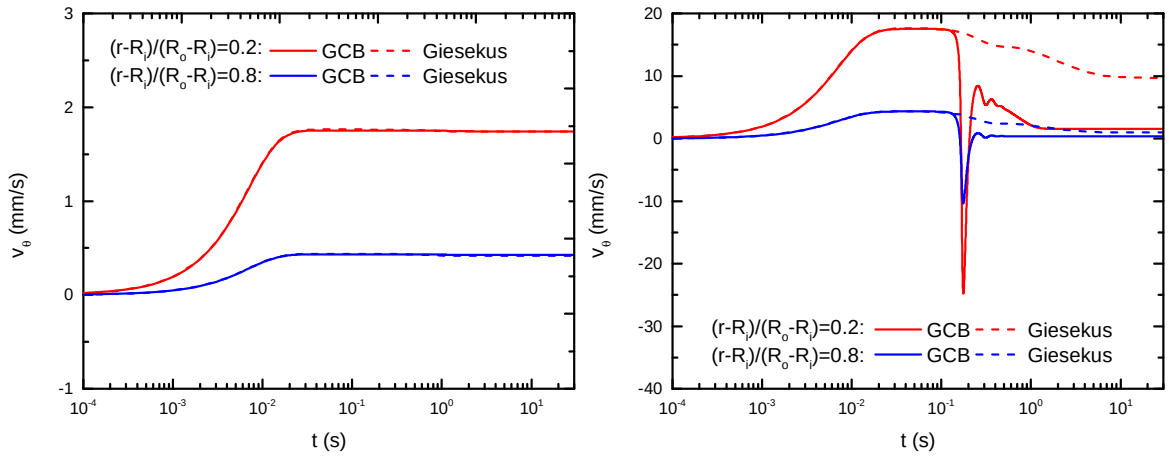

Figure 7: Azimuthal velocity versus time calculated for GCB model (solid lines) and Giesekus model (dashed lines) at two different radial positions in cylindrical gap. The shear rate corresponds to $\dot{\gamma} = 2.2\,\mathrm{s}^{-1}$ (left column) and $\dot{\gamma} = 22\,\mathrm{s}^{-1}$ (right column), respectively. A ramp-up rate of $a = 110\,\mathrm{s}^{-1}$ was used.

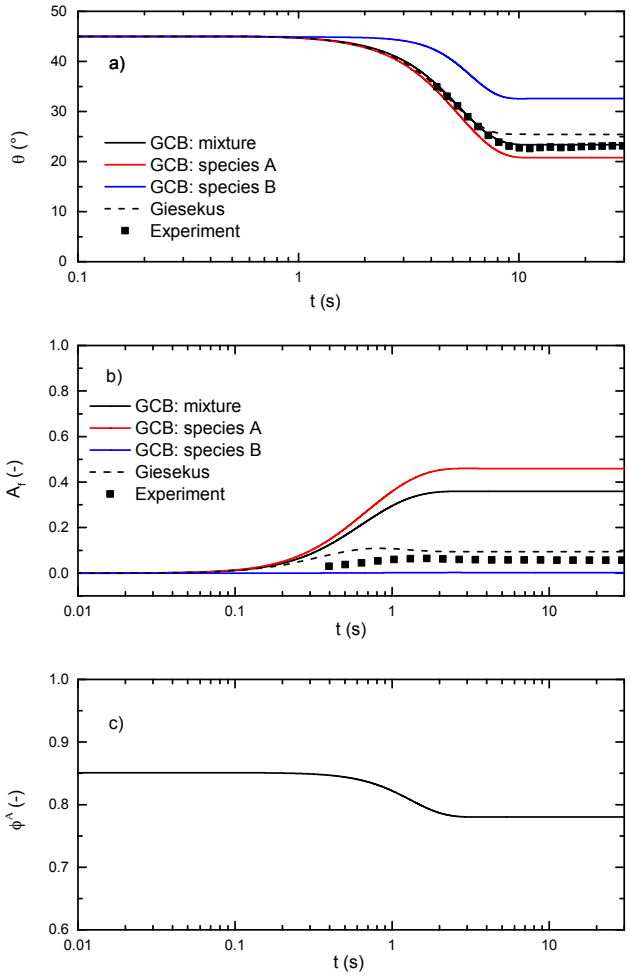

Figure 8: Temporal evolution of microstructural characteristics predicted by GCB model (solid lines) during transient shear flow ($\dot{\gamma} = 2.2\,\mathrm{s}^{-1}$). a) Orientation angle calculated for micellar mixture and individual species b) alignment factor calculated for micellar mixture and individual species, and c) concentration in mass fractions of species A. A ramp-up rate of $110\,\mathrm{s}^{-1}$ was used. The corresponding results calculated for the Giesekus model and the experimental data are indicated by dotted lines and filled squares, respectively.

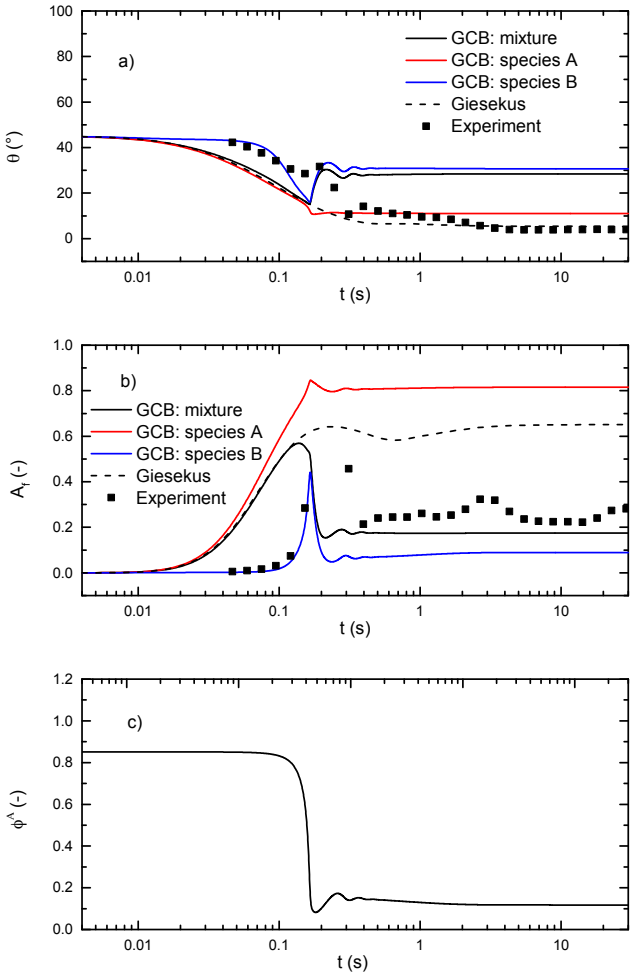

Figure 9: Temporal evolution of microstructural characteristics predicted by GCB model (solid lines) during transient shear flow ($\dot{\gamma} = 22\,\mathrm{s}^{-1}$). a) Orientation angle calculated for micellar mixture and individual species b) alignment factor calculated for micellar mixture and individual species, and c) concentration in mass fractions of species A. A ramp-up rate of $110\,\mathrm{s}^{-1}$ was used. The corresponding results calculated for the Giesekus model and the experimental data are indicated by dotted lines and filled squares, respectively.

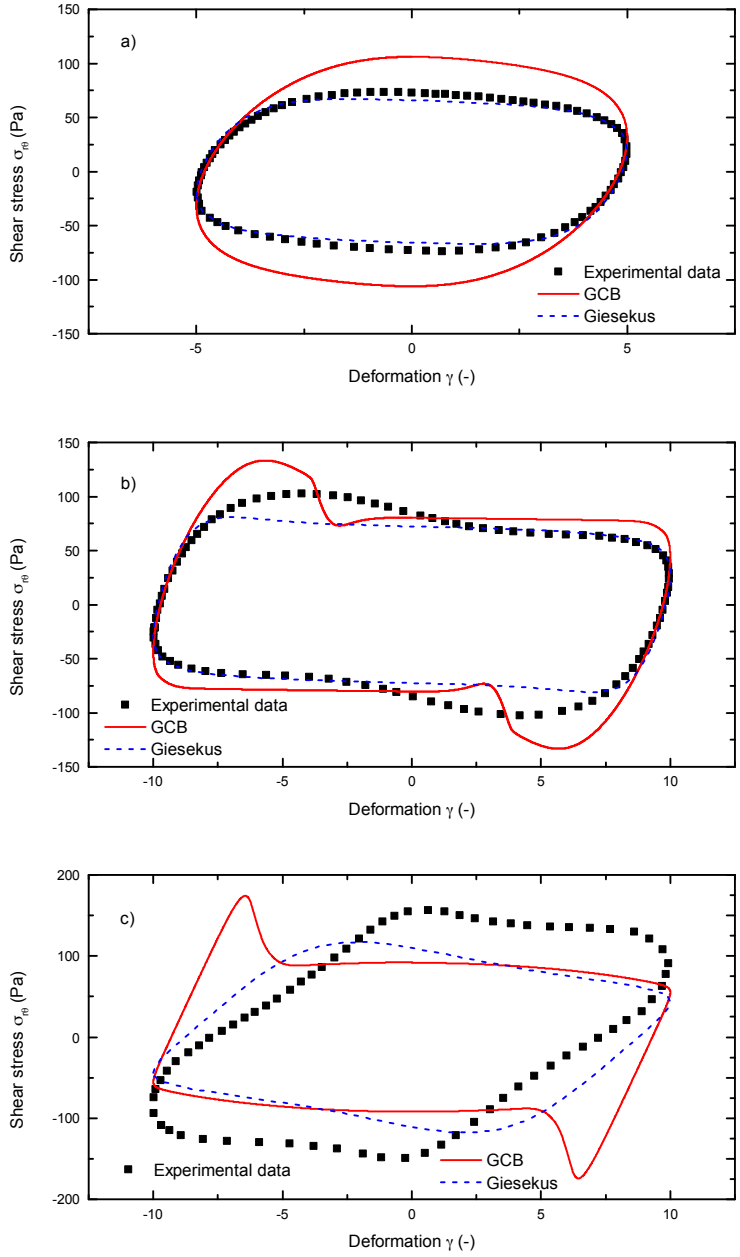

Figure 10: Elastic Lissajous-Bowditch curve calculated for GCB model (left column) and Giesekus model (right column) using three different conditions at the inner cylindrical wall. a) $\omega = 0.56\,\mathrm{rad/s}$ and $\gamma_0 = 5$, b) $\omega = 0.56\,\mathrm{rad/s}$ and $\gamma_0 = 10$, and c) $\omega = 5.6\,\mathrm{rad/s}$ and $\gamma_0 = 10$. Comparison between numerical solution (line) and experimental data (filled squares).

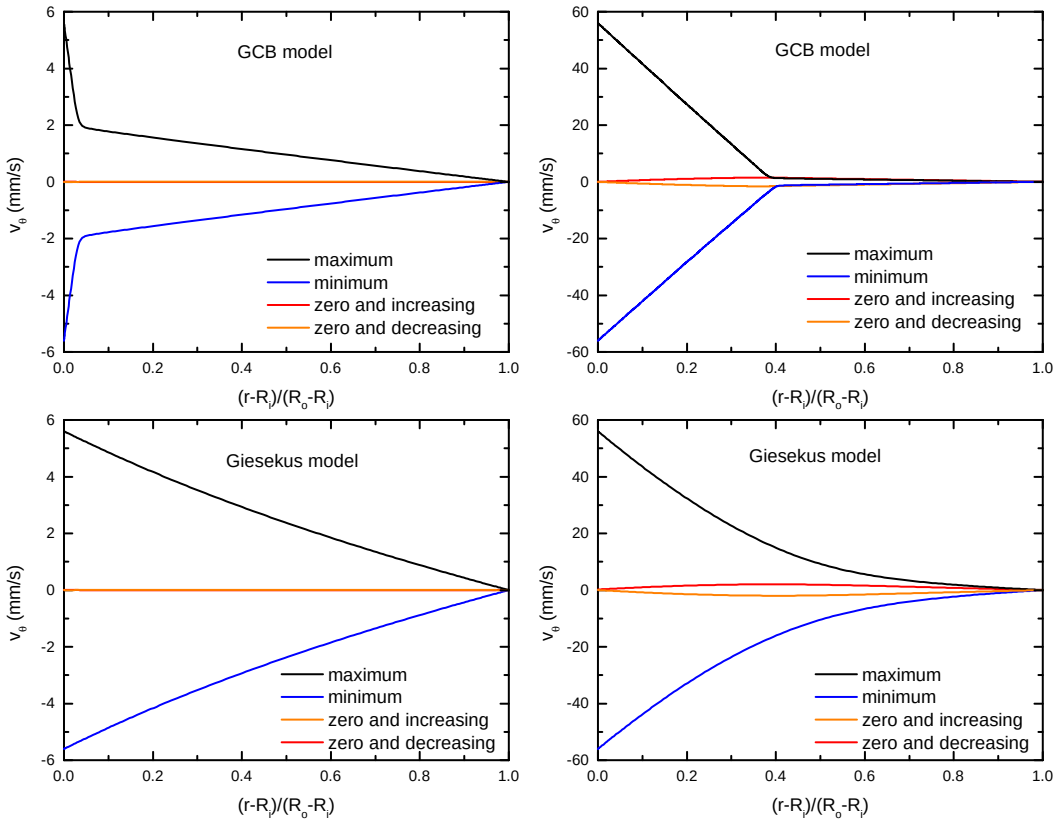

Figure 11: Azimuthal velocity across cylindrical gap predicted by GCB model (top row) and Giesekus model (bottom row). The profiles shown are at the instant when the wall velocity is maximum (black), minimum (blue), zero and increasing (red) , and zero and decreasing (orange), after all initial transients have decayed. The condition at the inner wall corresponds to $\omega = 0.56\,\mathrm{rad/s}$ and $\gamma_0 = 10$ (left column) and $\omega = 5.6\,\mathrm{rad/s}$ and $\gamma_0 = 10$ (right column), respectively.

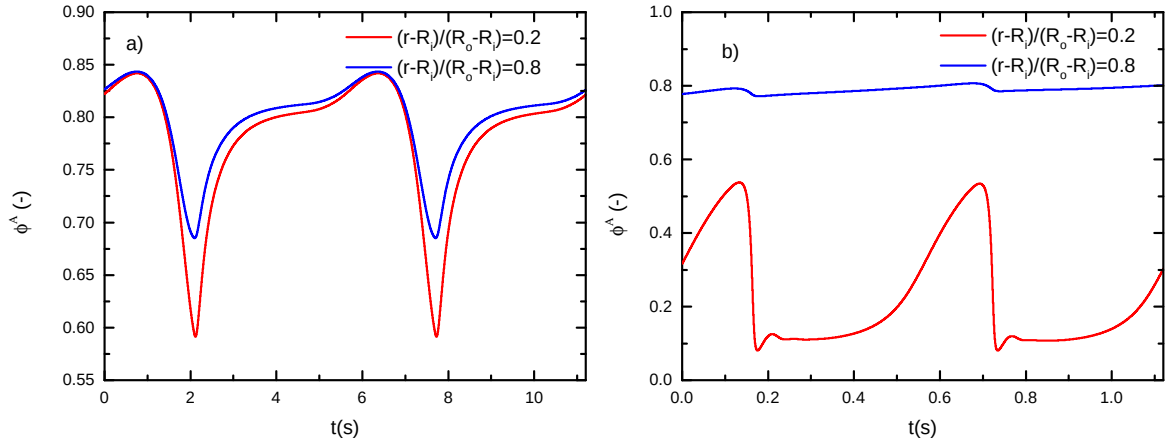

Figure 12: Concentration of species A versus time calculated for GCB model at two different positions in cylindrical gap. The condition at the inner cylinder corresponds to a) $\omega = 0.56\,\mathrm{rad/s}$ and $\gamma_0 = 10$ and b) $\omega = 5.6\,\mathrm{rad/s}$ and $\gamma_0 = 10$.

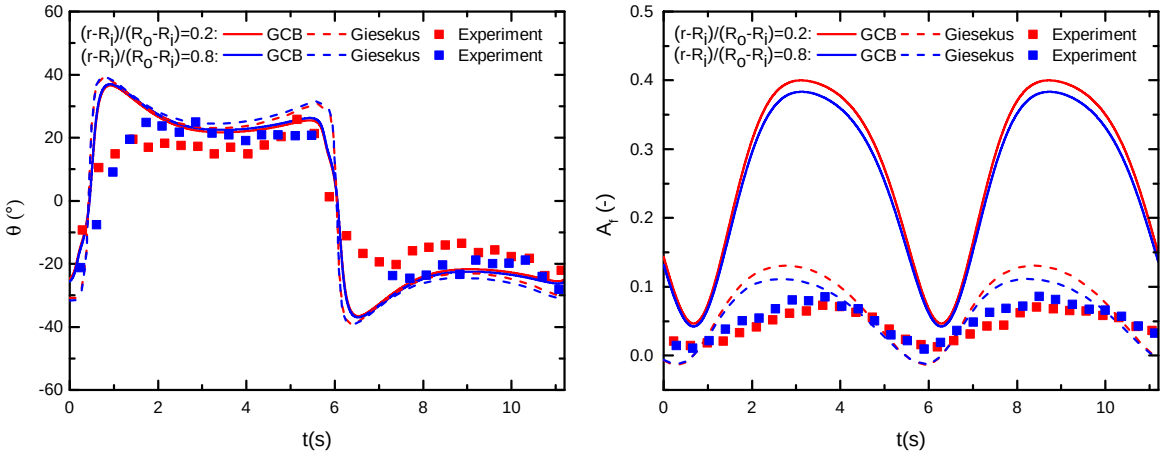

Figure 13: Temporal evolution of microstructural characteristics predicted by GCB model (solid lines) and Giesekus model (dashed lines) for $\omega = 0.56\,\mathrm{rad/s}$ and $\gamma_0 = 5$. a) Average orientation angle and b) alignment factor. The experimental data are represented by filled squares.

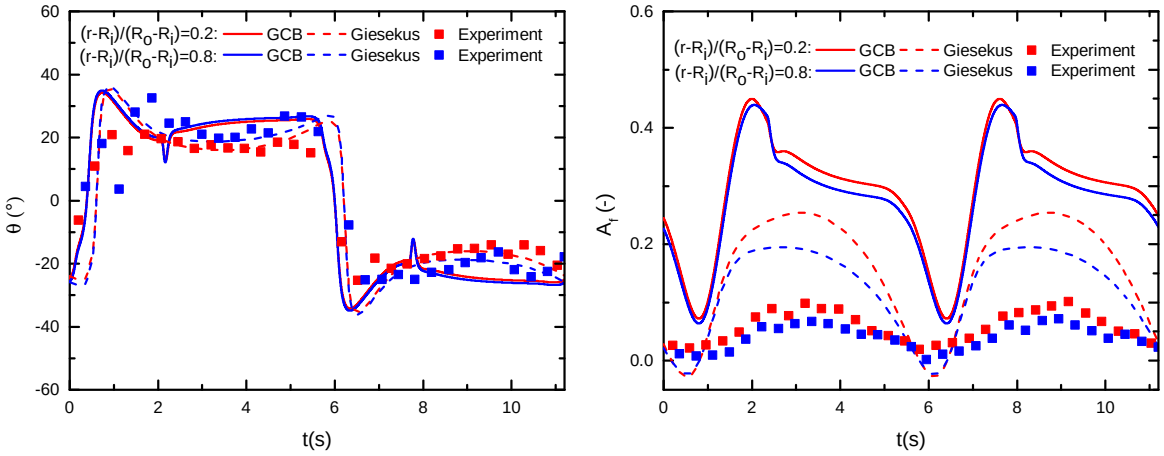

Figure 14: Temporal evolution of microstructural characteristics predicted by GCB model (solid lines) and Giesekus model (dashed lines) for $\omega = 0.56\,\mathrm{rad/s}$ and $\gamma_0 = 10$. a) Average orientation angle and b) alignment factor. The experimental data are represented by filled squares.

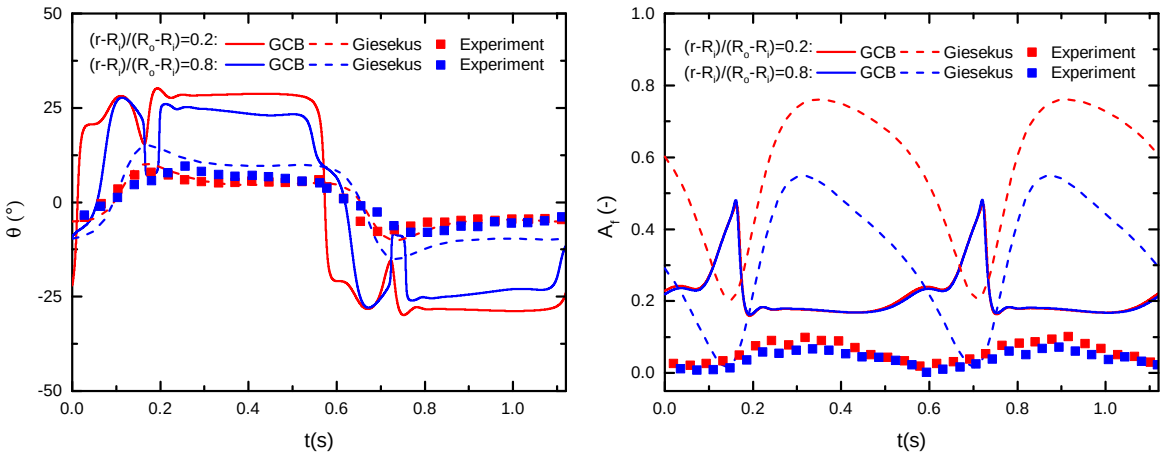

Figure 15: Temporal evolution of microstructural characteristics predicted by GCB model (solid lines) and Giesekus model (dashed lines) for $\omega = 5.6\,\mathrm{rad/s}$ and $\gamma_0 = 10$. a) Average orientation angle and b) alignment factor. The experimental data are represented by filled squares.